Materials Advances

ROYAL SOCIETY OF CHEMISTRY

PAPER

View Article Online
View Journal | View Issue

Cite this: *Mater. Adv.*, 2026, 7, 1604

Optimization of lead-free $BiFeO_3$ perovskite solar cells for efficient solar-energy conversion in futuristic green technologies

Muhammad Umar Salman * and Shahid Atiq *

Received 30th October 2025,
Accepted 8th December 2025

DOI: 10.1039/d5ma01257k

rsc.li/materials-advances

The adverse effects of global warming and our dependence on hazardous energy sources, like coal and petroleum, have shifted focus toward solar energy, a sustainable and clean solution. Perovskite materials, particularly $BiFeO_3$, are attracting attention as absorber layers due to their multifunctional properties. This study employs COMSOL to simulate 1D TiO_2/$BiFeO_3$/Spiro-OMeTAD solar cells with ideal ohmic contacts at different operating temperatures. Results demonstrate that the short-circuit current density increases with the $BiFeO_3$ thickness, and efficiency peaks at an optimal thickness. However, the maximum efficiency of 10.88% is achieved (in TiO_2/$BiFeO_3$/Spiro-OMeTAD) when the electron-transport layer's density of states in the valence and conduction bands (N_CN_V) is $\sim 2 \times 10^{16}$ cm^{-3}, while TiO_2/SnS/$BiFeO_3$/Spiro-OMeTAD shows the maximum efficiency of 20.99% at the SnS layer thickness of 700 nm. Moreover, an increase in $BiFeO_3$'s bandgap enhances the open-circuit voltage (V_{oc}) but reduces the fill factor. On the other hand, $BiFeO_3$'s N_CN_V has no significant impact on efficiency but shows inverse coupling with V_{oc}. Additionally, increasing $BiFeO_3$'s electron affinity improves the fill factor, while increasing TiO_2's and Spiro's electron affinities enhances the V_{oc} and power output, respectively. This work provides insights for optimizing material properties and device parameters in experimental applications and highlights the potential of $BiFeO_3$-based perovskites for next-generation photovoltaics.

1. Introduction

The global energy crisis can be addressed by solar energy, which is a sustainable, non-polluting, and inexhaustible source of energy.[1–3] For this purpose, the materials extensively studied for photovoltaic (PV) applications are organic, inorganic or hybrid perovskite solar cells (PSCs). Since 2009, these PSCs have demonstrated robust improvement in power conversion efficiency (η), increasing from 3.8% to approximately 26%.[4–6] PSCs have been identified as next-generation PV technology, surpassing the conventional solar cell; however, perovskites (PVKs) exhibiting strong ferroelectric (FE) response are particularly preferred.[7] Conventional solar cells are based on crystalline silicon (c-Si) technologies and operate through a single p–n junction mechanism with fixed material interfaces and well-defined efficiency limits determined by the Shockley–Queisser limit. They rely on established material and design parameters and have long served as performance benchmarks for evaluating emerging solar technologies. The inherent spontaneous polarization of FE materials facilitates the separation of the photogenerated electron–hole pairs without the development of the conventional n-type and p-type depletion regions. There are many factors that influence the PV nature of FE materials, including the Schottky barrier effect, bulk PV effect, and domain wall theory.[8–10] Specifically, the alignment of domains within the FE material induces polarization, which further produces the depolarization field. When the built-in field and depolarization field are aligned in the same direction, it promotes the efficient separation of electrons and holes.[11] The spontaneous polarization arises from the off-center and non-centrosymmetric displacement of positive and negative ions in the ABO_3 structure of FE materials.[12,13] Various PVK materials have been reported thus far, including $BaTiO_3$, $Bi_4Ti_3O_{12}$, and PZT.[14–17] However, the key limitation associated with these materials is their large bandgap (E_g), often exceeding 3 eV, which is not feasible for solar energy conversion under sunlight. This large E_g results from the high electronegativity difference between the B-site and oxygen atoms. Therefore, reducing the E_g is crucial to improve the η of FE materials in PV applications. Hence, bandgap engineering through the substitution of an appropriate metal cation at the B-site can alter both the FE response and E_g of FE materials. Thus, a completely new FE material for PV applications is needed, one having both high

Centre of Excellence in Solid State Physics, University of the Punjab, Lahore-54590, Pakistan. E-mail: muhammadumarsalmanm@gmail.com, satiq.cssp@pu.edu.pk

induced polarization and a small E_g. For this purpose, $BiFeO_3$ (BFO) has emerged as the potential candidate, as it not only fulfils these requirements but also is non-toxic.

BFO, a multiferroic material (rhombohedral symmetry, *R*3*c* space group), retains its multiferroicity above or at room temperature (RT), with a Curie temperature ($T_C \sim 1103$ K) and a G-type antiferromagnetic Néel temperature ($T_N \sim 643$ K). BFO is widely employed in magneto-electric, optoelectronic, multistate memory, and spintronic devices, due to its quite high remnant polarization (~ 100 μC cm^{-2}), which enables it to efficiently separate photogenerated electron–hole pairs.[18–23] At RT, BFO is stable and exhibits both magnetic and electric responses spontaneously, with a lower direct/indirect E_g (2.1–2.8/1.07 eV) and a high absorption coefficient ($\sim 10^5$ cm^{-1} at 400 nm).[24–32] The thin films of BFO exhibit lower series resistance, which promotes the enhanced collection of photogenerated charge carriers.[33] Notably, the switching of the photocurrent is achieved by simply switching the direction of spontaneous polarization. These properties render BFO a potential candidate among the other conventional PVK materials for optical and FE enhancements. Despite their large open circuit voltage (V_{oc}), BFO-based solar cells have a lower η than commercial Si-based cells. The highest experimentally reported η for BFO is 10% so far, though it can be improved by tuning the FE response and E_g.[34,35] There are many reasons for this low η, but the major limiting factors include high leakage currents and low magnetization, possibly due to oxygen vacancies, high volatilization of Bi, valence fluctuations in Fe ions, or the presence of secondary phases.[36–40] These factors lead to η values below the theoretical limits; however, BFO is the best choice for researchers because its ferroelectric and non-centrosymmetric natures enable polarization-driven charge separation through bulk and domain-wall photovoltaic effects.[41,42] Many strategies *i.e.* substitution or composite formation, have been done to resolve issues like conductivity, leakage current, and magnetization.[43,44] However, these approaches often lead to structural defects or secondary-phase occurrence.[45–49] In parallel, researchers are trying hard to improve these factors *via* a controlled synthesis process and the insertion of an electron-transport layer (ETL) or a hole-transport layer (HTL) across the BFO layer. Though effective, these layers result in interface defects and ultimately reduce the overall η of the solar cell. Recently, HTL-free solar cells have been proposed, which have fewer defects and are low in cost.[50] In BFO-based solar cells, TiO_2 has been widely employed as an ETL, owing to its ease of synthesis, low cost, excellent crystalline stability, anisotropic growth behavior, and efficient electron-transport characteristics.[51]

Extensive studies have been conducted by both experimental and theoretical groups, such as Kim *et al.* (2020), De Los *et al.* (2020), Karthick *et al.* (2020), Kumar *et al.* (2021), Sebastian *et al.* (2021), Singh *et al.* (2021) and Hossain *et al.* (2023).[52–58] However, no significant attention has been paid to the application of the most advanced mathematical-based solver to simulate BFO-based solar cells. In this study, we make use of the most advanced COMSOL Multiphysics simulation software to simulate the 1D TiO_2/BFO/Spiro-OMeTAD heterojunction solar cell—a novel approach that has not been explored for the enhancement of device performance. This software allows us to vary multiple factors simultaneously, offering deep insights to improve η. The software is based on the finite element method (FEM), which solves Poisson's equation and drift-diffusion partial differential equations using semiconductor physics. It allows the coupling of more than one physics simultaneously, enabling 3D simulation of complex devices. Based on advanced mathematical methods, the accuracy of this software can be estimated by comparing the simulated output values, which normally show a difference of only 1.50% and 2.40% from the experimental data.[59] The sole purpose of this simulation-based study is to optimize the parameters efficiently, improving the overall performance of the cell. Excellent optimization of parameters affords improved output results from the device, and advanced tools of simulation enable this process. This includes the optimization of the doping type, doping level, carrier concentration, defect type, defect density, layer thickness, metal contacts, *etc.* Once the parameters are optimized, we simulate the solar cell to find out its output characteristics, including current density–voltage (*J*–*V*) and power–voltage (*P*–*V*) curves for the determination of η and other quantities.

2. Numerical modeling

In this study, the COMSOL Multiphysics software was employed as a robust tool to analyze the underlying causes of low η in solar cells. While earlier investigations primarily utilized 1D or 2D simulation frameworks to study the basic characteristics of similar devices, the present work implements a 3D COMSOL-based model to capture realistic spatial effects and provide more accurate performance predictions. It forecasts the electrical behavior and internal physical mechanics of the structure as a physics-based 2D and 3D device simulator. It achieves this by solving fundamental equations, including Poisson's equation and carrier continuity equations, which establish a relationship between electrostatic potential and carrier densities.[60] For charge-transport analysis, the Drift-Diffusion Model emerges as the most effective and computationally efficient approach. Poisson's equation, which relates the electrostatic potential to the local space charge density, is expressed as (eqn (1)):

$$\nabla.(\varepsilon\nabla\Psi) = -\rho \quad (1)$$

where, Ψ denotes the electrostatic potential, ε represents the local permittivity, and ρ signifies the local space charge density.[61] The steady-state continuity equations (eqn (2) and (3)) for electron and hole transport are described as follows:

$$\frac{\partial n}{\partial t} = \frac{1}{q}\nabla \cdot \vec{J}_n + G_n + R_n \quad (2)$$

$$\frac{\partial p}{\partial t} = -\frac{1}{q}\nabla \cdot \overrightarrow{J}_p + G_p + R_p \quad (3)$$

where, $\vec{J}_n$ and $\vec{J}_p$ represent the current densities for the electrons and holes, respectively, and G_n and G_p denote the generation rates of charge carriers. R_n and R_p represent the total recombination rates in Gaussian and tail states, respectively, whereas the electron charge is represented by q.[62] The term G, governing the rate of photogenerated electron–hole pairs, was incorporated in COMSOL to simulate light absorption across the active layer and is expressed as $G = \alpha I_0 e^{-\alpha x}$. Here, α is the absorption coefficient, I_0 represents the incident light intensity, and x is the penetration depth. In the Drift-Diffusion model, the current densities are related to the quasi-Fermi levels, as follows (eqn (4) and (5)):

$$\vec{J}_n = -q\mu_n n \nabla \phi_n \quad (4)$$

$$\vec{J}_p = -q\mu_p p \nabla \phi_p \quad (5)$$

where, μ_n and μ_p denote the mobilities of electrons and holes, respectively, while ϕ_n and ϕ_p represent the quasi-Fermi levels. Using the Boltzmann approximation, the quasi-Fermi levels are further linked to the electrostatic potential and carrier concentrations, as follows (eqn (6) and (7)):

$$n = n_i \exp\left(\frac{\psi - \phi_n}{k_B T}\right) \quad (6)$$

$$p = n_i \exp\left(\frac{\psi - \phi_p}{k_B T}\right) \quad (7)$$

where, T is the lattice temperature, k_B is the Boltzmann constant, and n_i represents the effective intrinsic carrier concentration.[63] The electrical properties of the device are computed based on the defined physical structure and applied bias conditions. This involves discretizing the governing equations (Poisson's equation and carrier continuity equations) over a finite element grid, which divides the simulation domain into a set of nodes and grid points. By solving these equations across the grid, the carrier transport mechanisms within the structure are accurately modeled. This finite-element approach enables a comprehensive simulation of the solar cell's performance.[64]

The simulation of the TiO_2/$BiFeO_3$/Spiro-OMeTAD solar cell was performed in COMSOL using a systematic approach. First, the 1D geometry of the device, including the TiO_2 electron-transport layer, $BiFeO_3$ absorber, and Spiro-OMeTAD hole-transport layer, was defined with precise thicknesses. Material properties, such as the bandgap, electron affinity, carrier mobility, and permittivity, were assigned based on reported values. Ideal ohmic contacts were applied at the electrodes, and a fine mesh was generated throughout the solar cell structure, with increased density at the interfaces between the TiO_2/$BiFeO_3$ and $BiFeO_3$/Spiro-OMeTAD layers to accurately capture variations in the carrier concentration and the electric field. The semiconductor physics module solved the coupled Poisson, continuity, and drift-diffusion equations to model charge transport and carrier generation. Illumination with the AM1.5 solar spectrum provided the photo-generation rate in the absorber layer, and a cross-sectional area of 4×10^{-12} m^2 was used. Steady-state simulations were performed for varying thicknesses, transport-layer properties, and operating temperatures. Finally, current density–voltage (J–V) characteristics were extracted, ensuring a thorough evaluation of the device performance.

3. Device simulation and methodology

3.1. Solar absorption and solar spectrum

The solar spectrum represents the distribution of solar energy across different wavelengths. Fig. 1(a) shows that solar irradiance increases sharply to a peak of about 1.6 Wm^{-2} nm^{-1} at 460 nm. Beyond this point, it gradually declines up to 2500 nm due to the combined effects of the decreasing solar blackbody emission intensity at longer wavelengths and the absorption by atmospheric gases, such as water vapor, oxygen, and carbon dioxide. This demonstrates the wavelength-dependent nature of solar irradiance, where shorter wavelengths exhibit stable intensity and longer wavelengths show a progressive decrease.[65] The refractive index (n) and extinction coefficient (k) are critical parameters that define a material's optical properties, both of which exhibit wavelength-dependent variations. The n parameter initially increases with the wavelength due to the dispersion phenomenon, where light bending intensifies as it interacts with the material, and for wavelengths beyond 0.4 μm, n begins to decrease, stabilizing at longer wavelengths (above 1 μm), as shown in Fig. 1(b). In contrast, k initially decreases with increasing wavelength, particularly beyond 0.3 μm. This behavior arises from the electronic transitions within the material, reflecting its distinct interaction with incident light, and beyond 0.5 μm, k stabilizes, indicating minimal further absorption. The interplay of n and k demonstrates their influence on light transmission, reflection, and absorption in the material.[66] The generation of electron–hole (e/h) pairs is governed by the interaction of

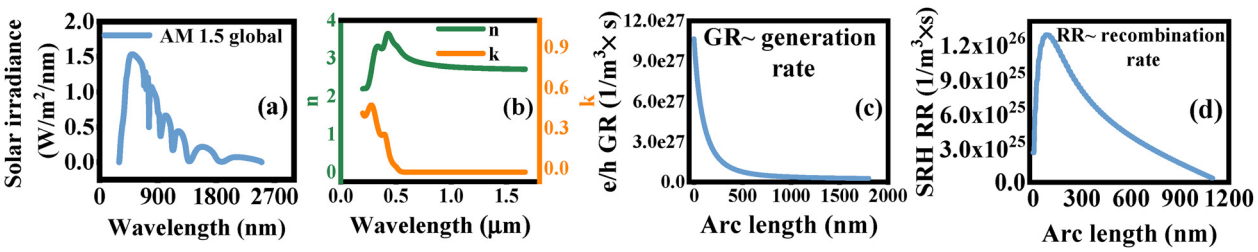

Fig. 1 (a) Solar spectrum, (b) n and k dependence on wavelength, (c) generation rate of e/h pairs inside the layers of solar cell, and (d) Shockley-Read-Hall recombination rate within the device.

incident light with the material, and when photons are absorbed, electrons transition from the valence band to the conduction band, creating e/h pairs.[67] In Fig. 1(c), the arc length indicates the total thickness of the optimized layers in this solar cell device. The e/h pair generation is maximum within the 100 to 500 nm arc length, approximately, signifying the high absorption and carrier generation. Beyond 500 nm, the generation rate declines and stabilizes, implying less pair generation for longer arc lengths. This behavior underscores the critical role of arc length in maximizing the photo-generated carrier densities.[68]

After generation, the Shockley–Read–Hall (SRH) recombination occurs, a process which involves electron–hole recombination facilitated by material defects or impurities and also exhibits wavelength-dependent characteristics. At smaller arc lengths, the SRH recombination peaks, reaching a maximum value of approximately 1.3×10^{26} ($1/m^3 \times s$) at around 100 nm, as shown in Fig. 1(d). With increasing arc length, the SRH recombination rate declines sharply, highlighting its sensitivity to changes in the arc length. This reduction is attributed to variations in the carrier concentrations and the density of trapping centers that modulate the recombination dynamics. The observed trends emphasize the critical interplay between recombination mechanisms and material properties under varying spectral conditions.[69]

3.2. Energy band structure

Fig. 2(a and b) presents the architecture of a multi-layer PV cell comprising TiO_2/BFO/Spiro-OMeTAD as its primary constituents, and each layer in this design is chosen for its unique properties to optimize solar-light absorption, charge separation, and efficient carrier transport, ultimately enhancing the device's power-generation efficiency.[70] The operation of this device is supported by the material-specific characteristics and semiconductor physics, both of which have been extensively studied and validated in this study. The TiO_2 layer, positioned at the top, serves as the ETL due to its wide E_g and high electron mobility. These properties render TiO_2 highly transparent to sunlight, allowing most incident photons to penetrate the underlying BFO layer for absorption.

Materials with increased thickness exhibit enhanced absorption of low-energy photons due to their large penetration depth. Conversely, high-energy photons, such as those in the near-ultraviolet spectrum, exhibit high absorption coefficients, resulting in reduced penetration depths. Fig. 2(c) shows the conduction band level (E_c) and the Fermi level for electrons (E_{fn}), indicating that energy remains constant as the material thickness increases, up to approximately 75 nm. Beyond this threshold, the energy begins to rise, reaching a value of 2.88 eV, and for thinner materials, the absorption of higher-energy photons predominates due to their shorter penetration depths. In contrast, low-energy photons in the near-infrared region exhibit lower absorption coefficients, allowing deeper penetration into the material. The relationship between the Fermi level for holes (E_{fp}) and the valence band level (E_v) demonstrates that the carrier energy initially starts at low negative values and gradually increases, reaching zero as the energy levels align. The E_g energies of the studied materials vary significantly: spiro materials exhibit the highest E_g energy, followed by BFO with an intermediate E_g, and TiO_2 with the lowest E_g energy. These variations highlight the distinct electronic properties of these materials at varying thicknesses.[71] The observed trends suggest a direct correlation between the material thickness and E_g energy: as the thickness increases, the E_g energy also rises. This behavior underscores the influence of material geometry on its optical and electronic properties, emphasizing the importance of thickness-dependent optimization for tailored PV or optoelectronic performance.

Moreover, TiO_2 effectively facilitates electron transport to the top contact while minimizing electron–hole recombination, a critical factor for maintaining charge separation. The BFO layer, a multiferroic PVK with an E_g of 2.2 eV, acts as the main light-absorbing component of the device. BFO absorbs photons across a significant portion of the visible spectrum, leading to the generation of excitons upon photoexcitation.[34] The FE properties of BFO aid in separating these excitons, directing electrons toward the TiO_2 and holes toward the bottom HTL, Spiro-OMeTAD, and this transportation is shown in Fig. 2(d). Spiro-OMeTAD, positioned at the bottom of the cell, works as the HTL, facilitating hole transport from the BFO layer to the bottom contact.[72] By ensuring efficient hole transport and suppressing recombination with electrons, this layer supports sustained charge separation and a steady flow of electric current. The functionality of this PV cell is governed by the

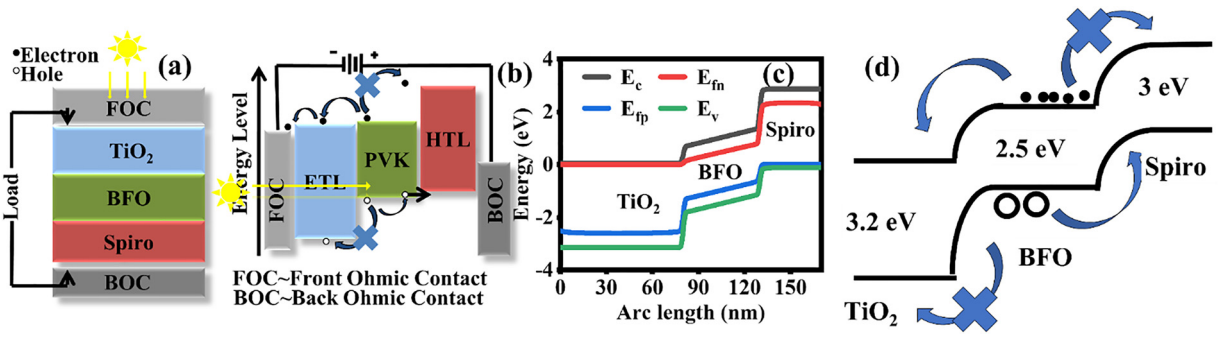

Fig. 2 (a) Solar cell's schematic, (b) schematic with energy levels, (c) energy-level variations *vs.* arc length, and (d) energy-band alignment of the TiO_2/BFO/Spiro-OMeTAD heterojunction solar cell for the transportation of charge carriers.

principles of semiconductor band theory, particularly the energy-band alignment among the layers. The alignment between BFO and Spiro-OMeTAD supports downward hole transport, while the wide E_g of TiO_2 prevents electron recombination, directing electrons toward the top contact.

Although a dedicated interfacial recombination analysis was not presented as a separate section, its impact is inherently embedded within the simulated current–voltage characteristics and directly contributes to the observed current saturation behavior. The interfacial regions between adjacent layers were modeled under charge-neutral conditions, with a surface charge density of 0 C cm^{-2}, thereby eliminating artificial fixed charges and maintaining electrostatic equilibrium across the junctions. To accurately describe recombination dynamics at these interfaces, the SRH trapping mechanism was employed, assigning both electron and hole surface recombination velocities of 1000 cm s^{-1}. These parameters fall within the experimentally reported ranges for perovskite and oxide-based heterojunctions, ensuring physically consistent interfacial kinetics. The trap energy level was positioned at the midgap, corresponding to a neutral defect state with zero offset from the intrinsic Fermi level, thereby representing symmetric recombination for electrons and holes. Furthermore, the interface continuation feature in COMSOL Multiphysics was enabled to preserve numerical convergence and physical continuity across the heterointerfaces, ensuring reliable simulation of interfacial charge transport and recombination phenomena.

The properties of TiO_2, BFO, and Spiro-OMeTAD enable effective photon absorption, charge carrier separation, and transport within the multi-layer PV cell. Careful band alignment and material selection, as supported by extensive research in PV technology, contribute to a highly efficient system capable of converting solar energy into electricity with reduced recombination losses. The optimized input parameters for the TiO_2, BFO, and Spiro-OMeTAD materials, assuming the ideal ohmic front and back contacts, are tabulated in Table 1.

4. Results and discussion

4.1. Effect of BFO's thickness on PV performance

The absorbing layer, such as BFO, acts as the active region of the solar cell and helps to generate the photo-induced charge carriers, which further migrate towards their respective electrodes. For this, the thickness of the absorbing layer is very crucial because as the thickness increases, the absorption of light may increase, ultimately enhancing the photo-induced charge carriers. But, on the other hand, after this optimum thickness is achieved, the performance of the solar cell may decrease because of the increase in the internal resistance and defect density. Fig. 3(a) presents a schematic illustration to visualize the effect of the thickness of the absorbing layer, and it is obvious that increasing the thickness of this layer beyond its optimal value may increase the number of defects, as depicted by the small circle. Fig. 3(b) shows the *J–V* characteristics of the solar cell for different BFO thicknesses, where J_{sc} increases with increasing BFO thickness. At 50 nm, J_{sc} is around 3.69 mA cm^{-2}, while at 1850 nm, it reaches approximately 9.004 mA cm^{-2}, indicating improved charge collection for thicker layers. The sharp decline occurs at different voltages, with the thinner layers dropping at around 1.6–2.0 V and the thicker layers at around 1.3 V, suggesting that increased thickness lowers V_{oc} due to the higher recombination losses. Fig. 3(c) shows *P–V* curves for different BFO thicknesses, where the maximum power density increases with thickness. Thinner layers peak around 1.6–2.0 V, while thicker layers peak near 1.3–1.5 V, showing that increasing the thickness enhances power generation, but excessive thickness may cause recombination losses, affecting efficiency.

Fig. 3(d) presents the variation in J_{sc}, V_{oc}, and P_{max} at different thicknesses of BFO, and it shows that by varying the thickness from 50 to 1850 nm, the J_{sc} exhibits a steady increase with thickness, rising from 3.697 mA cm^{-2} at 50 nm to a maximum of 9.004 mA cm^{-2} at 1850 nm. This behavior is a result of the enhanced photon absorption as thickness increases, which facilitates the generation of a greater number of charge carriers, and the contribution of longer-wavelength photons becomes significant at larger thicknesses, further boosting J_{sc}. Furthermore, V_{oc} decreases from 2.178 V at 50 nm to 1.994 V at 1400 nm, then remains constant up to 1850 nm. This indicates that increasing the BFO thickness initially increases the recombination losses, but beyond 1400 nm, its impact stabilizes. On the other hand, the P_{max} of 53.485 W at 50 nm increases to 104.5 W at 631 nm and then declines to 95.79 W at 1850 nm. The rise in P_{max} up to 631 nm results from the optimal photon absorption and minimal recombination losses, and beyond this thickness, higher recombination rates and defect densities limit the charge-carrier generation, reducing P_{max}. Moreover, Fig. 3(e) shows the fill factor (FF) and efficiency (η) dependence on the BFO thickness, and FF gradually decreases from 66.39% (at 50 nm) to 53.40% (at 1850 nm). Conversely, as the BFO thickness increases, the η of the solar cell reaches a maximum at an optimal thickness and decreases beyond this point. At 50 nm, the η is 5.34%, increasing to a peak value of 10.101% at 500 nm. Beyond this optimal thickness, the η decreases to 9.579% at 1850 nm. The increase in η up to the optimal thickness is attributed to the enhanced photon absorption, particularly for photons with longer wavelengths, leading to improved charge-

Table 1 Initial parameters of the materials used for the respective layers in 1D TiO_2/BFO/Spiro OMeTAD PSC

Material properties	TiO_2	BFO	Spiro-OMeTAD
Thickness (nm)	80	50	40
Energy bandgap (eV)	3.2	2.5	3
Electron affinity (eV)	3.9	3.3	1.9
Relative permittivity	9	6	3
C.B effective density of states 'N_C' (cm^{-3})	1×10^{20}	5×10^{18}	1×10^{20}
V.B effective density of states 'N_V' (cm^{-3})	2×10^{20}	5×10^{18}	1×10^{20}
Electron mobility 'μ_n' ($cm^2\ V^{-1}\ s^{-1}$)	20	80	2
Hole mobility 'μ_h' ($cm^2\ V^{-1}\ s^{-1}$)	25	25	1×10^{-2}
Electron lifetime, SRH, (ns)	1	1	5
Hole lifetime, SRH, (ns)	1	1	5
Ref.	73	74	75

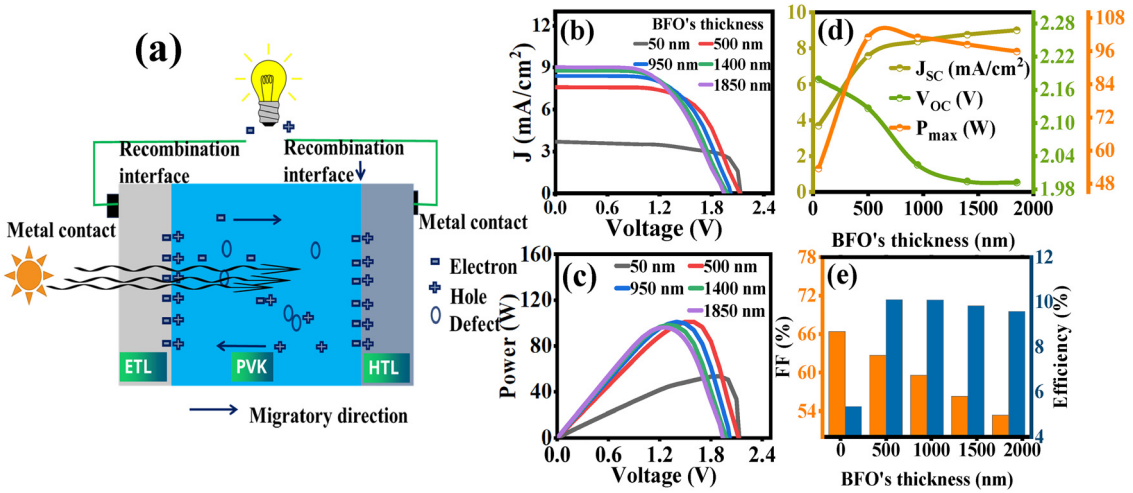

Fig. 3 (a) Schematic of the effect of the absorbing layer's thickness on the performance of the solar cell, (b) *J*–*V* curve and (c) *P*–*V* curve of the TiO_2/BFO/Spiro-OMeTAD solar cell, and the effect of BFO's thickness variation on (d) J_{sc}, V_{oc}, P_{max}, and (e) %FF and %efficiency.

Table 2 Designed device (1D TiO_2/BFO/Spiro-OMeTAD) performance parameters with varying thickness of the absorber layer (BFO)

BFO's thickness (nm)	J_{sc} (mA cm^{-2})	V_{oc} (V)	P_{max} (W)	FF (%)	Efficiency (%)
50	3.697	2.179	53.485	66.392	5.349
500	7.578	2.127	101.018	62.676	10.102
950	8.373	2.024	100.957	59.571	10.095
1400	8.758	1.994	98.319	56.295	9.831
1850	9.004	1.992	95.794	53.405	9.5793

carrier generation. However, beyond 500 nm, the η decreases due to the increased recombination rates, which reduce charge-carrier lifetimes and limit charge-carrier generation.[76] All the output characteristics for different BFO thicknesses are listed in Table 2.

4.2. Effect of the ETL's thickness variation on the PV performance

A thinner ETL is best for achieving the maximum output yield of solar cells. An increase in the layer thickness may cause hindrance to the incident light that must reach the absorbing layer, and secondly, the increase enhances the series resistance of the solar cell. Fig. 4(a) presents the schematic illustration of the working mechanism of the solar cell having a thinner ETL, and it is clear that the incident light can reach the active region of the solar cell easily. But, if the ETL is thicker, it stops the incident light, as depicted in Fig. 4(b). Fig. 4(c) illustrates the *J*–*V* response at different ETL thicknesses, ranging from 10 to 150 nm, and J_{sc} decreases with increasing ETL thickness. The sharp J_{sc} drop occurs at 1.6 V for all thicknesses, indicating relatively high resistance and recombination losses for thicker ETLs. The *P*–*V* response is used to determine the P_{max} of solar cells, as shown in Fig. 4(d), and the power peaks at around 100.95 W at an ETL thickness of 10 nm and decreases to 56.76 W at 150 nm. Thinner layers achieve high power, while thicker layers exhibit reduced output due to increased resistance; P declines sharply within the 1.6–2.0 V range. It is observed that a thinner ETL improves electron transport and light absorption, maximizing current density, while thicker layers hinder these processes by increasing resistance and reducing light penetration.

Fig. 4(e) shows the variation in J_{sc}, V_{oc}, and P_{max} at different thicknesses of ETL. J_{sc} decreases from 7.57 to 4.420 mA cm^{-2}, and similarly, the V_{oc} decreases (from 2.126 to 2.063 V) as thickness increases (from 10 to 150 nm), suggesting that the V_{oc} is sensitive to the ETL thickness, with optimal performance achieved by the thinner layer. Thinner ETL layers help maintain better voltage due to efficient charge transport, while thicker layers introduce more resistance, resulting in a reduced value of voltage. Moreover, P_{max} decreases (101.01 to 56.76 W) with increasing ETL thickness due to the increased recombination and resistive losses. Fig. 4(f) depicts the variation in %FF and η. FF decreases from 62.67% at 10 nm to its lowest at 45 nm, then gradually increases to 62.23% at 150 nm. This suggests that a moderate ETL thickness increases the resistance and recombination rate, but thicker layers stabilize FF. On the other hand, a consistent decline can be seen in the overall η as the ETL thickness increases. This is because thinner ETLs ensure efficient charge transport, minimal recombination, and better light penetration, while thicker layers impede performance due to the increased resistance, increased recombination rate, and reduced photon absorption by the active layer.[77] The detailed numerical values for these output characteristics for different ETL thicknesses are listed in Table 3.

4.3 Effect of HTL's thickness variation on the PV performance

The effect of shunt resistance in solar cell's performance is remarkable, specially it affects the V_{oc}, and it can be understood in this sense, as HTL thickness increases it provides unwanted paths to the internal current and due to which shunt resistance decreases and it ultimately reduces the V_{oc}, as shown in Fig. 5(a and b). Furthermore, the *J*–*V* and *P*–*V* characteristics at different

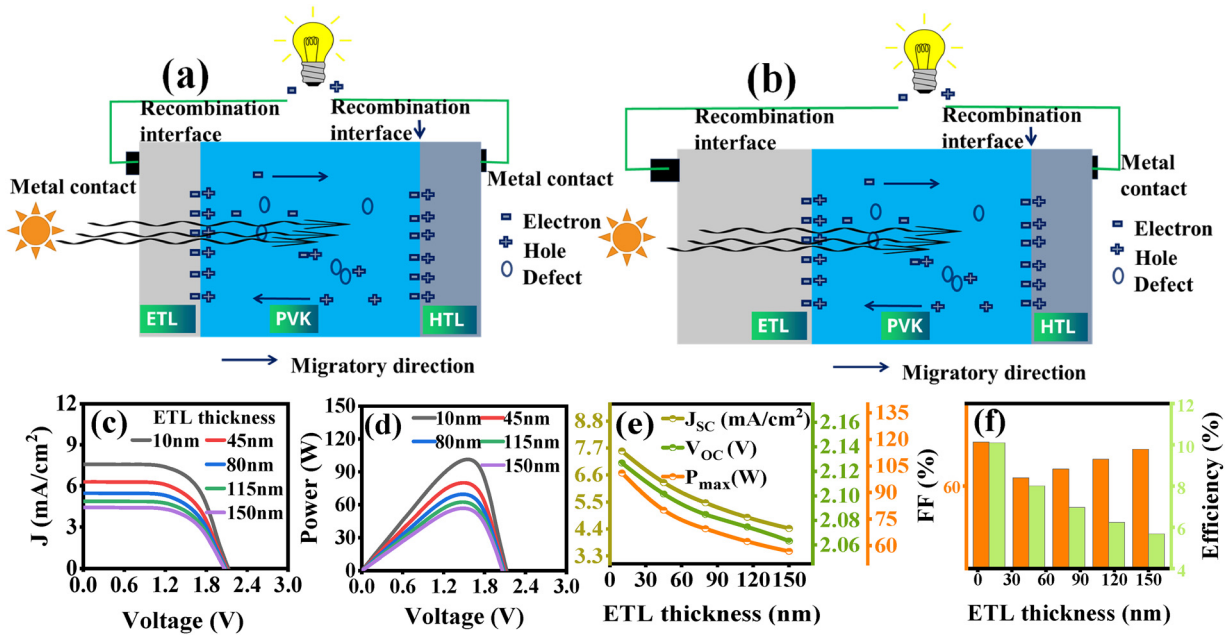

Fig. 4 Schematic of the effect of the ETL's thickness on the performance of solar cells: (a) thinner ETL and (b) thicker ETL. (c) *J*–*V* curve and (d) *P*–*V* curve of the TiO_2/BFO/Spiro-OMeTAD solar cell. Effect of the ETL's thickness variation on (e) J_{sc}, V_{oc}, P_{max}, and (f) %FF and %efficiency.

Table 3 Designed device (1D TiO_2/BFO/Spiro-OMeTAD) performance parameters with varying thickness of the ETL (TiO_2)

TiO_2's thickness (nm)	J_{sc} (mA cm^{-2})	V_{oc} (V)	P_{max} (W)	FF (%)	Efficiency (%)
10	7.578	2.126	101.017	62.673	10.101
45	6.295	2.101	80.035	60.492	8.003
85	5.466	2.084	69.559	61.028	6.955
115	4.876	2.074	62.335	61.619	6.233
150	4.420	2.063	56.76	62.230	5.676

HTL thicknesses, ranging from 50 to 150 nm, were examined to determine the J_{sc}, V_{oc}, and P_{max}, as shown in Fig. 5(c) and (d), respectively. J_{sc} remains nearly constant before sharply dropping, while *P* increases, before a sharp decline at 1.6 V; both parameters show minimal variation across different HTL thicknesses. Fig. 5(e) presents the variation in J_{sc}, V_{oc}, and P_{max}, and J_{sc} increases from 7.57 mA cm^{-2} at 10 nm to 7.74 mA cm^{-2} at 150 nm due to the improved charge collection and reduced carrier recombination with increasing HTL thickness, enhancing the current extraction efficiency. On the other hand, V_{oc} exhibits a gradual decrease (from 2.1268 to 2.1058 V) with increasing HTL thickness (from 10 to 150 nm), likely resulting from an energy level mismatch and the shunt resistance in the thicker layers. Moreover, P_{max} increases as the thickness increases, peaking at 103.45 W at an HTL thickness of 150 nm, and may saturate after this optimal thickness is achieved. Furthermore, FF improves with increasing HTL thickness up to the optimum range, and finally, η increases steadily from 10.10% to 10.34%, as shown in Fig. 5(f). These findings underscore the critical role of HTL-thickness optimization in achieving a balance between efficient charge transport and resistive losses, and a properly tuned HTL thickness enhances the overall device performance, achieving the maximum η and power output for PSCs.[78] Table 4 presents a comprehensive overview of all these output characteristics for different HTL thicknesses.

4.4. Effect of BFO's DOS in the conduction and valence bands (N_CN_V) on the PV performance

It is important to study the density of states (DOS) in the conduction and valence bands, because it is directly linked to the carrier's transportation and recombination process. Fig. 6(a) shows the higher DOS at conduction band, reflecting the greater probability of intra-band transition, which is non-radiative emission of energy and this happens beyond an optimal level, but its probability is lesser under the optimum range of DOS. Similarly, the higher DOS in the valence band leads to a greater probability of intra-band transitions, as shown in Fig. 6(b). Fig. 6(c) shows that as N_CN_V increases from 2×10^{17} to 2×10^{20} cm^{-3}, J_{sc} remains nearly constant, but the V_{oc} at which it sharply drops shifts to lower values, indicating an increase in the recombination and a reduction in the charge-extraction efficiency. Fig. 6(d) illustrates the *P*–*V* characteristics. *P* initially rises, peaks, and then declines at higher voltages. The shifting peak suggests that higher N_CN_V values influence the recombination dynamics, impacting the optimal operating voltage and reducing the overall power extraction.

In Fig. 6(e), although J_{sc} slightly increases from 8.158 mA cm^{-2} to 8.185 mA cm^{-2}, V_{oc} significantly decreases from 1.99 V to 1.235 V, resulting in a reduction in P_{max} from 87.21 W to 59.117 W. The decrease in V_{oc} with an increase in the effective density of states strongly confirms their inverse relationship, highlighting a fundamental trade-off in device performance. This occurs because the higher density of states enhances

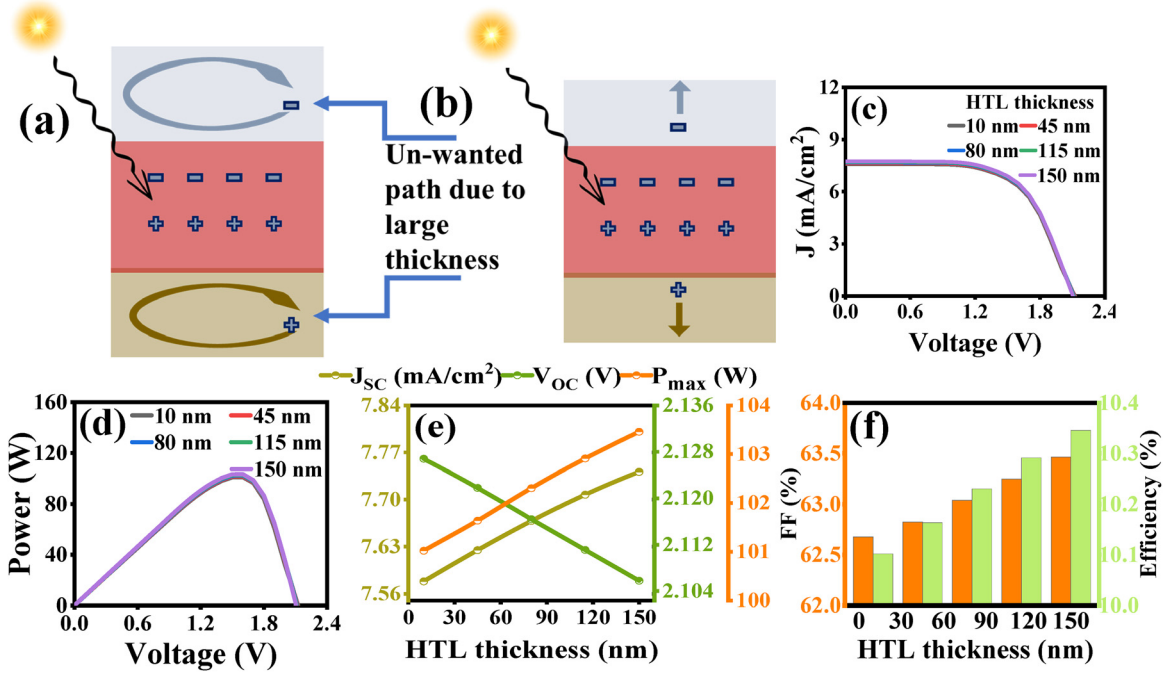

Fig. 5 (a and b) Schematic of the effect of thicker and thinner HTLs on the performance of solar cells. (c) *J*–*V* curve and (d) *P*–*V* curve of the TiO_2/BFO/Spiro-OMeTAD solar cell. Effect of the HTL's thickness variation on (e) J_{sc}, V_{oc}, P_{max}, and (f) %FF and %efficiency.

Table 4 Designed device (1D TiO_2/BFO/Spiro-OMeTAD) performance parameters with varying thickness of the HTL (spiro)

Spiro's thickness (nm)	J_{sc} (mA cm^{-2})	V_{oc} (V)	P_{max} (W)	FF (%)	Efficiency (%)
50	7.578	2.126	101.019	62.676	10.102
150	7.624	2.121	101.638	62.823	10.163
80	7.668	2.116	102.304	63.037	10.230
115	7.707	2.111	102.912	63.248	10.291
150	7.741	2.105	103.457	63.464	10.345

recombination losses, which reduces the built-in potential and the V_{oc}, while the slight improvement in J_{sc} due to increased carrier generation cannot compensate for the major voltage drop, leading to a decrease in the maximum power.[79] In Fig. 6(f), the FF increases from 53.68% to 58.47%, indicating improved charge extraction and reduced resistive losses at higher N_CN_V values. However, η decreases from 8.72% to 5.91%, mainly due to the significant drop in V_{oc} and P_{max}, which outweighs the benefits of the FF improvement. This suggests that an excessive increase in N_CN_V leads to increased recombination, negatively impacting overall performance. Table 5 presents the influence of N_CN_V variations on the overall device performance, showing trends in the electrical characteristics and η as the density of states increases.

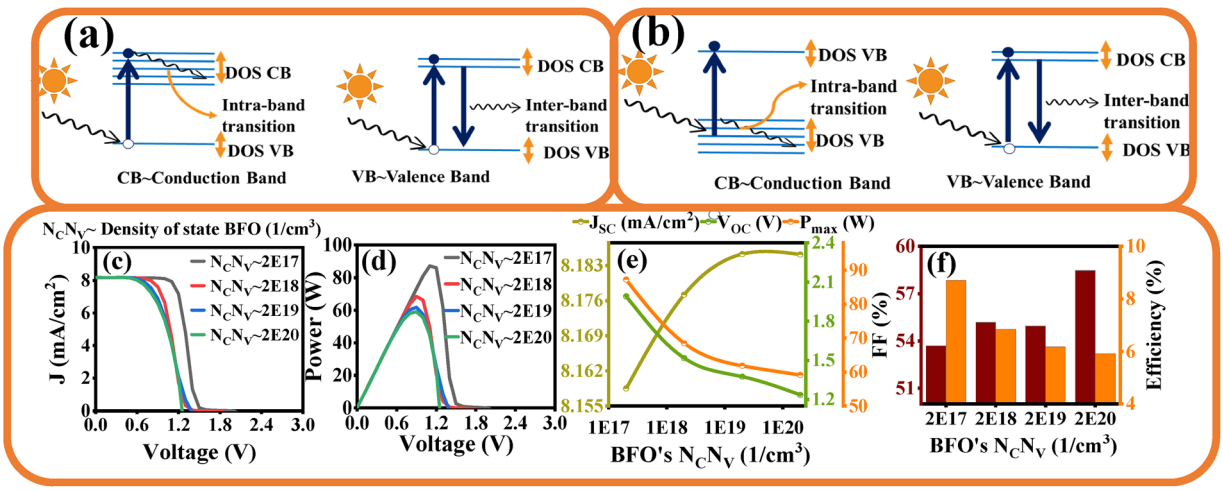

Fig. 6 (a and b) Schematic of the higher and lower density of states (DOS) in the conduction & valence bands (N_CN_V) within the $BiFeO_3$ (BFO) layer. (c) *J*–*V* curve and (d) *P*–*V* curve of the TiO_2/BFO/Spiro-OMeTAD solar cell. Effect of BFO's N_CN_V on (e) J_{sc}, V_{oc}, P_{max}, and (f) %FF and %efficiency.

Table 5 Designed device (1D TiO_2/BFO/Spiro-OMeTAD) performance parameters with varying density of states of BFO in the conduction and valence bands (N_CN_V)

BFO's N_CN_V (cm^{-3})	J_{sc} (mA cm^{-2})	V_{oc} (V)	P_{max} (W)	FF (%)	Efficiency (%)
2×10^{17}	8.158	1.991	87.216	53.721	8.721
2×10^{18}	8.177	1.517	68.468	55.187	6.846
2×10^{19}	8.185	1.375	61.854	54.954	6.185
2×10^{20}	8.185	1.235	59.117	58.476	5.911

Table 6 Designed device (1D TiO_2/BFO/Spiro-OMeTAD) performance parameters with varying density of states of TiO_2 in the conduction and valence bands (N_CN_V)

TiO_2's N_CN_V (cm^{-3})	J_{sc} (mA cm^{-2})	V_{oc} (V)	P_{max} (W)	FF (%)	Efficiency (%)
2×10^{15}	8.194	1.357	60.871	54.727	6.087
2×10^{16}	7.713	2.108	108.877	66.940	10.887
2×10^{17}	7.750	2.115	105.899	64.575	10.589
2×10^{18}	7.670	2.119	104.556	64.315	10.455
2×10^{19}	7.668	2.120	103.353	63.552	10.335
2×10^{20}	7.668	2.114	101.784	62.781	10.178

4.5. Effect of ETL's DOS in the conduction and valence bands (N_CN_V) on the PV performance

Fig. 7(a) illustrates the *J–V* characteristics for different TiO_2 density of states (N_CN_V). As N_CN_V increases from 2×10^{15} to 2×10^{18} cm^{-3}, J_{sc} remains stable at lower voltages but drops sharply at higher voltages. Higher N_CN_V shifts the cutoff point, affecting the V_{oc} and indicating changes in charge transport and recombination. Fig. 7(b) presents the *P–V* characteristics for varying TiO_2'N_CN_V. *P* increases, peaks, and then declines. A higher DOS shifts the peak position and alters the maximum power, highlighting its effect on the solar cell performance.

Fig. 7(c) shows the variations in J_{sc}, V_{oc}, and P_{max}. As N_CN_V increases from 2×10^{15} cm^{-3} to 2×10^{20} cm^{-3}, J_{sc} decreases from 8.194 mA cm^{-2} to 7.6 mA cm^{-2} and then stabilizes, due to the saturation of the charge carrier transport. V_{oc} increases from ~1.35 V to ~2.1 V, indicating improved band alignment with minimal effect at higher N_CN_V, while P_{max} increases from ~60.87 W to ~108.87 W and then levels off as the recombination counteracts further gains. Moderate N_CN_V values enhance performance, but excessive values lead to saturation. Fig. 7(d) shows the variation of FF and η with the N_CN_V in TiO_2. FF increases from 54% to 66%, stabilizing or presenting a slight decline afterward due to improved charge transport. Moreover, η follows a similar trend, rising from 6.08% to 10.88%, then plateauing as further increases no longer significantly enhance performance.[80] The improvement is due to the reduced recombination loss and better carrier collection, although excessively high values lead to diminishing returns. Table 6 highlights the impact of the ETL's N_CN_V variations on the solar cell performance, showcasing key trends and dependencies.

4.6. Effect of BFO's electron affinity (χ) on the PV performance

The energy-band alignment is crucial for the efficient operation of solar cells; any discontinuity or misalignment can lead to erroneous results. Therefore, ensuring proper energy-band alignment across the three layers requires careful optimization of the electron affinity. χ refers to the energy difference between the vacuum energy level and the conduction band minimum of a material. It governs the energy-band alignment at the heterojunction interfaces and significantly affects charge transfer and recombination dynamics within the solar cell. Therefore, its optimization is essential for achieving efficient carrier transport and high device performance. For the influence of varying the χ values of the absorber layer (BFO) on the operation performance of the solar cell, *J–V* characteristics show, in Fig. 8(a), that J_{sc} remains nearly constant, while the V_{oc} drop shifts with χ. At 3.3 eV, the drop starts around 0.9 V, at 3.4 eV around 1.0 V, and at 3.5 eV beyond 1.2 V, showing that higher χ improves charge transport, reducing voltage losses. In Fig. 8(b), the *P–V* characteristics display that *P* increases with the voltage, peaks, and then declines, with the highest peak occurring at 3.3 eV, while 3.4 eV and 3.5 eV show lower peaks, indicating that lower χ values favor maximum power output.

Furthermore, Fig. 8(c) presents the variations in J_{sc}, V_{oc}, and P_{max} at different χ values, and it is clear that J_{sc} increases slightly from 8.171 mA cm^{-2} at 3.3 eV to 8.179 mA cm^{-2} at 3.5 eV, indicating improved charge extraction with higher χ values. V_{oc} first decreases from 1.81 V at 3.3 eV to 1.77 V at 3.4 eV, then increases to 1.83 V at 3.5 eV, suggesting an initial rise in recombination at 3.4 eV before the improvement in band alignment at 3.5 eV improves voltage. P_{max} continuously decreases from 78 W to 55 W, implying that increasing χ introduces losses that outweigh the gains in charge transport, reducing overall device performance. However, FF decreases significantly from 55.40% to 38.98%, indicating that higher χ negatively impacts charge extraction and increases resistive

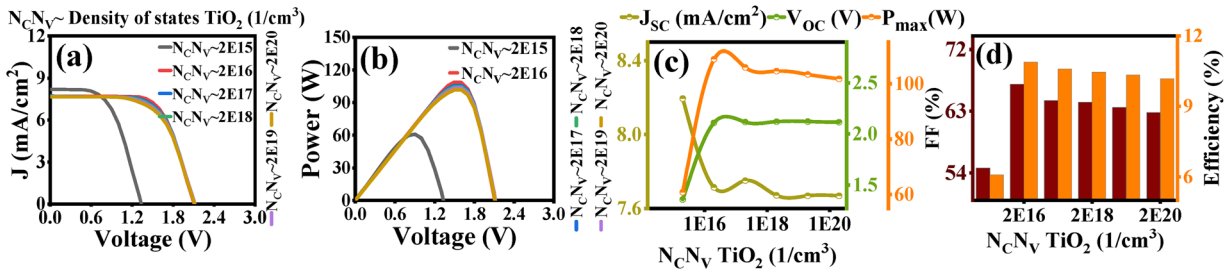

Fig. 7 Effect of the density of states within the conduction and valence bands (N_CN_V) in the electron-transport layer (TiO_2) on the solar cell performance. (a) *J–V* curve and (b) *P–V* curve of the TiO_2/BFO/Spiro-OMeTAD solar cell. Effect of TiO_2's N_CN_V on (c) J_{sc}, V_{oc}, P_{max}, and (d) %FF and %efficiency.

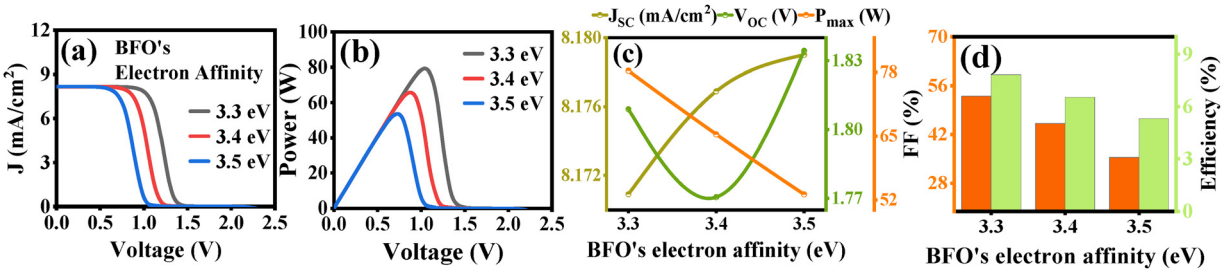

Fig. 8 (a) *J*–*V* curve and (b) *P*–*V* curve of the TiO_2/BFO/Spiro-OMeTAD solar cell. Effect of $BiFeO_3$ (BFO)'s electron affinity on (c) J_{sc}, V_{oc}, P_{max}, and (d) %FF and %efficiency.

Table 7 Designed device (1D TiO_2/BFO/Spiro-OMeTAD) performance parameters with varying electron affinity of BFO

BFO's affinity (eV)	J_{sc} (mA cm^{-2})	V_{oc} (V)	P_{max} (W)	FF (%)	Efficiency (%)
3.3	8.170	1.808	78.317	52.987	7.831
3.4	8.176	1.770	65.361	45.147	6.536
3.5	8.179	1.834	53.127	35.411	5.312

losses. Similarly, η declines from 8.50% to 5.80%, which follows the trend of decreasing P_{max} shown in Fig. 8(d). This η reduction is directly linked to energy-band misalignment, leading to compromised charge extraction and an increased recombination rate.[76] In the end, all the output characteristics with varying BFO's electron affinities are listed in Table 7.

4.7. Effect of TiO_2's electron affinity (χ) on the PV performance

The performance of a solar cell is significantly influenced by the χ of the TiO_2 layer, and the variations in this parameter impact key electrical characteristics. Fig. 9(a) shows the *J*–*V* characteristics for different χ values of TiO_2 (3.5 eV to 3.7 eV). The sharp drop in *J* occurs around 1.6 V, indicating the turn-off point. The overall J_{sc} remains relatively stable before this V_{oc}, suggesting minimal impact of χ on the current generation until a critical voltage is reached. Fig. 9(b) illustrates the *P*–*V* curve for different TiO_2 electron affinities, where *P* rises, peaks, and then drops sharply. The peak power remains nearly constant, indicating the minimal impact of the electron affinity on the power output. However, slight differences may be attributed to changes in charge transport and recombination dynamics within the device.

Fig. 9(c) depicts the variations in J_{sc}, V_{oc}, and P_{max} with changing χ values. J_{sc} fluctuates within a narrow range of 8.1685 to 8.1700 mA cm^{-2}, showing a peak around 3.6 eV, while dipping at intermediate values, which indicates that specific electron affinities enhance charge extraction, improving current generation. V_{oc} follows the same pattern as J_{sc}, ranging between 1.49 V and 1.53 V, reaching its maximum at 3.6 eV. This behavior suggests that band alignment at these electron affinities optimally supports voltage generation. P_{max} remains relatively stable, fluctuating slightly between 48.801 W and 48.785 W, as the compensatory effects of J_{sc} and V_{oc} balance the overall power output. The observed trends indicate that optimizing electron affinity is crucial for enhancing solar cell performance without significantly affecting power stability. Fig. 9(d) indicates the variation of FF and η with TiO_2's electron affinity. FF ranges between 39.90% and 38.90%, reaching its highest values around 3.5 eV, and similarly, η peaks at 4.884% for 3.5 eV. When χ is optimal, the conduction band alignment enhances electron flow, reducing recombination losses and thereby increasing η. These findings emphasize the critical role of optimizing TiO_2's χ to balance energy alignment, minimize recombination, and enhance charge transport, to achieve superior solar cell performance.[81] Finally, the output values with varying electron affinities of TiO_2 are listed in Table 8.

4.8. Effect of Spiro's electron affinity (χ) on the PV performance

Fig. 10(a) illustrates the *J*–*V* curve, where J_{sc} remains constant (8.167 mA cm^{-2}) up to 0.6–1.1 V before decreasing to near-zero

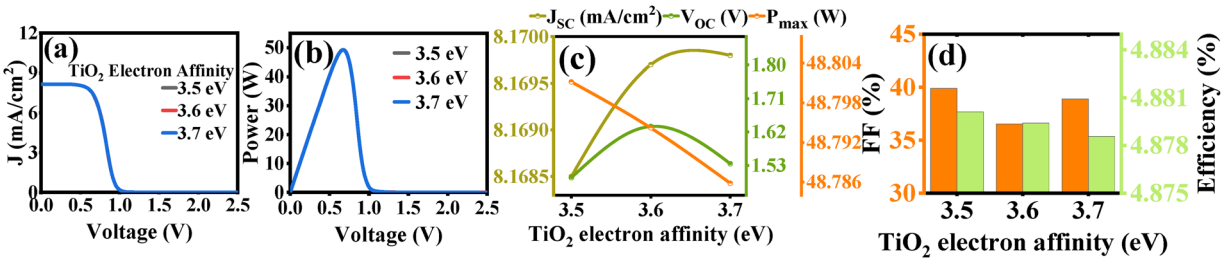

Fig. 9 (a) *J*–*V* curve and (b) *P*–*V* curve of the TiO_2/BFO/Spiro-OMeTAD solar cell. Effect of the electron affinity of TiO_2 on (c) J_{sc}, V_{oc}, P_{max}, and (d) %FF and %efficiency.

Table 8 Designed device (1D TiO_2/BFO/Spiro-OMeTAD) performance parameters with varying electron affinity of TiO_2

TiO_2's affinity (eV)	J_{sc} (mA cm^{-2})	V_{oc} (V)	P_{max} (W)	FF (%)	Efficiency (%)
3.5	8.168	1.497	48.801	39.903	4.880
3.6	8.169	1.634	48.794	36.531	4.879
3.7	8.169	1.534	48.785	38.909	4.878

Table 9 Designed device (1D TiO_2/BFO/Spiro-OMeTAD) performance parameters with varying electron affinity of Spiro

Spiro's affinity (eV)	J_{sc} (mA cm^{-2})	V_{oc} (V)	P_{max} (W)	FF (%)	Efficiency (%)
1.5	8.168	1.750	48.789	34.113	4.878
1.6	8.169	1.845	55.760	36.978	5.576
1.7	8.169	1.849	62.733	41.514	6.273
1.8	8.169	1.925	70.483	44.799	7.048
1.9	8.169	1.804	78.326	53.136	7.832

at higher voltages. This is attributed to the better energy-level alignment, enhancing photon-to-electron conversion. Fig. 10(b) demonstrates the *P*–*V* curve, with *P* increasing to a peak (78.32 W) as χ rises from 1.5 to 1.9 eV. Fig. 10(c) presents the variation in J_{sc}, V_{oc}, and P_{max} for different χ values of Spiro, and it is observed that J_{sc} increases from 8.167 to 8.169 mA cm^{-2} with rising χ, due to the improved symmetry in the energy levels and the enhanced charge carrier flow across the device. On the other hand, V_{oc} initially increases then slightly decreases as χ increases, attributable to the minimized bandgap mismatches between the absorber and HTL layers, which slightly diminish the charge-separation efficiency. However, P_{max} improves linearly from 48.78 to 78.32 W. These enhancements result from the improved energy-level alignment between the HTL and the PVK layer, which minimizes energy losses and charge-transport efficiency. Similarly, FF and η increase as shown in Fig. 10(d), and FF increases from 34.11 to 53.13%, while η increases from 4.878% at χ = 1.5 eV to 7.832% at χ = 1.9 eV. These results highlight the critical role of the HTL electron affinity in optimizing the performance of PSCs.[82] In the end, Table 9 presents a comprehensive overview of all the above-mentioned output characteristics with varying electron affinities of Spiro-OMeTAD.

4.9. Effect of operating temperature on the PV performance

The operating temperature of a solar cell significantly influences its performance, primarily by intensifying phonon vibrations, which, in turn, increase internal resistances, such as the cell's series resistance. Elevated temperatures also raise the likelihood of collisions between charge carriers and lattice ions, thereby amplifying recombination losses. Fig. 11(a) shows that an increase in the temperature of the device enhances the random motion of charge carriers inside the layers of solar cells, and at low temperatures, the random motion reduces, as shown in Fig. 11(b).

Furthermore, Fig. 11(c and d) shows the *J*–*V* and *P*–*V* characteristics at different operating temperatures, ranging from 290 to 310 K, for the determination of J_{sc}, V_{oc}, and P_{max} of the solar cell. Both *J* and *P* show a slight decline with temperature, but they sharply decrease at the V of 0.6 V. In Fig. 11(e), J_{sc} exhibits minimal variation with temperature changes, although a slight decrease is observed at higher temperatures. Similarly, V_{oc} reduces from 1.57 to 1.48 V as temperature increases from 290 to 310 K, and this decline is attributed to bandgap narrowing and an increase in the reverse saturation current, both of which negatively impact the device's ability to maintain a high V_{oc} at elevated temperatures. Moreover, P_{max} declines from 49.67 to 43.69 W, due to diminished FE polarization and increased recombination losses at higher temperatures, which collectively limit the charge-extraction efficiency. However, FF initially decreases and then increases to 36.01% as the temperature increases from 290 to 295 K, stabilizing thereafter, as shown in Fig. 11(f). This transient improvement is linked to enhanced carrier mobility and reduced series resistance, which temporarily offset the adverse effects of higher recombination rates. The η value of the solar cell slightly decreases from 4.96% to 4.36% with increasing temperature, as shown in Fig. 11(f). This is attributable to the intrinsic narrow bandgap properties and moderate FE behavior of the PVK material, which mitigate significant performance degradation under thermal variations.[83] Finally, all the output characteristics with varying temperatures of the operating device are tabulated in Table 10.

4.10. Effect of SnS's thickness on the PV performance of the TiO_2/SnS/BFO/Spiro-OMeTAD solar cell

Fig. 12(a) shows the *J*–*V* characteristics of the TiO_2/SnS/BFO/Spiro-OMeTAD solar cell for different SnS absorber thicknesses.

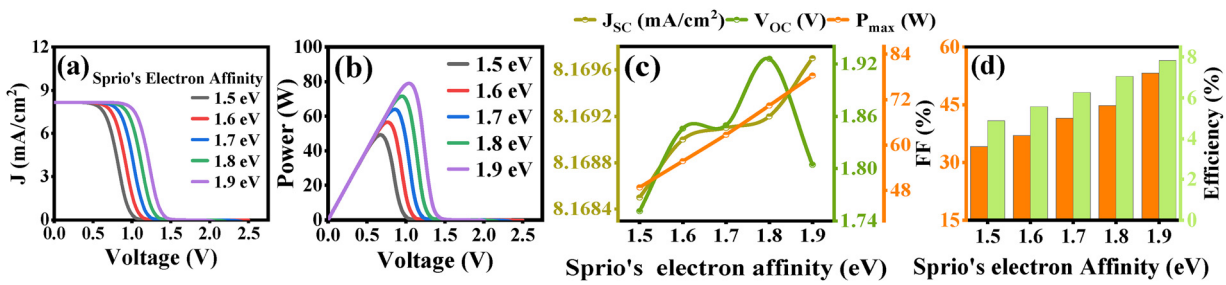

Fig. 10 (a) *J*–*V* curve and (b) *P*–*V* curve of the TiO_2/BFO/Spiro-OMeTAD solar cell. Effect of Spiro's electron affinity on (c) J_{sc}, V_{oc}, P_{max}, and (d) %FF and %efficiency.

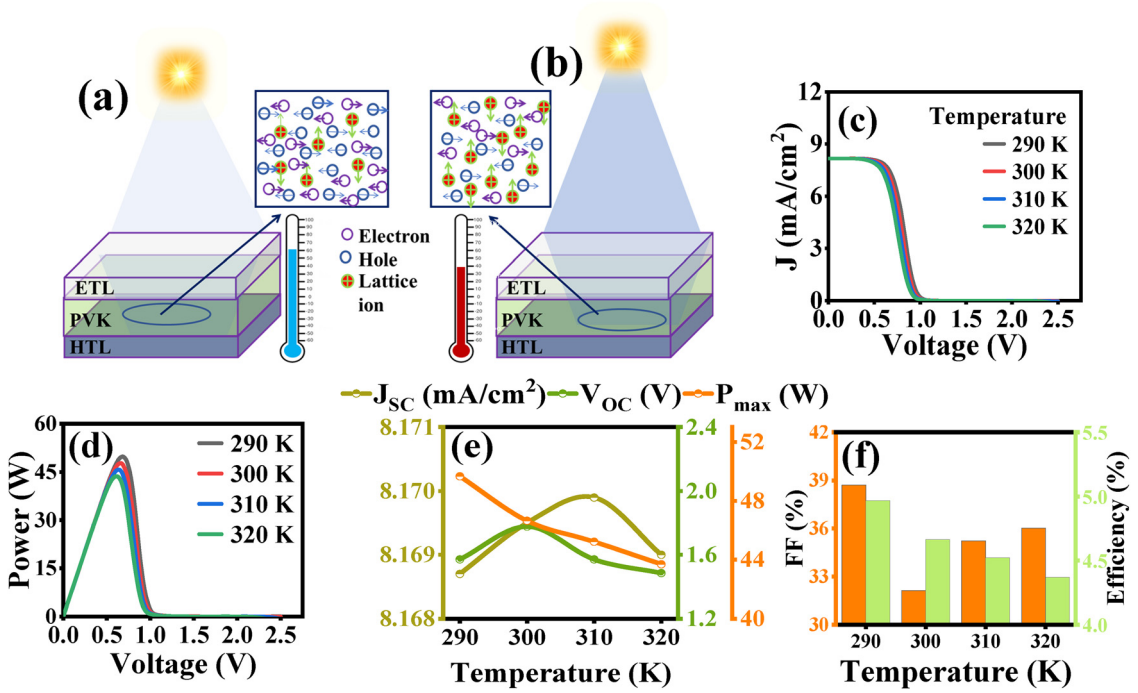

Fig. 11 (a) Higher temperature and (b) lower temperature effect on the device's internal environment. (c) J–V curve and (d) P–V curve of the TiO_2/BFO/Spiro-OMeTAD solar cell. Effect of temperature on (e) J_{sc}, V_{oc}, P_{max}, and (f) %FF and %efficiency.

J_{sc} increases with the thickness due to enhanced photon absorption and efficient charge generation. However, at higher thicknesses, a noticeable voltage drop occurs near the open-circuit region, indicating increased recombination and reduced carrier-collection efficiency in the thicker absorber layer. Fig. 12(b) presents the P–V characteristics for varying SnS absorber thicknesses. The output power increases with the thickness up to 700 nm, indicating enhanced light absorption and efficient charge-carrier extraction, which result in increased P_{max}. However, at 1000 nm, a noticeable voltage drop occurs near the maximum power region, leading to a decline in the power output. This reduction is primarily due to the increased series resistance, longer carrier transport paths, and enhanced recombination in the thicker absorber layer, which collectively lower the overall conversion efficiency. Fig. 12(c) shows the variation of J_{sc}, V_{oc}, and P_{max} with different SnS thicknesses. J_{sc} increases steadily from 31.02 to 31.98 mA cm^{-2} as the thickness rises from 100 nm to 700 nm, which is attributed to the enhanced optical absorption and a high generation rate of charge carriers within the active region. However, at 1000 nm, J_{sc} slightly drops to 31.45 mA cm^{-2} due to enhanced bulk recombination and limited carrier diffusion in the thicker layer. The V_{oc} remains nearly constant around 0.80–0.81 V throughout the thickness range, showing that it is primarily governed by the built-in potential and interface quality rather than the absorber thickness. P_{max} follows a similar trend to J_{sc}, increasing from 196.16 to 209.95 W up to 700 nm, indicating efficient charge extraction and minimal resistive losses. Beyond this point, it decreases to 155.68 W at 1000 nm because of the increased series resistance and recombination effects, which reduce the overall power conversion capability.

Table 10 Designed device (1D TiO_2/BFO/Spiro-OMeTAD) performance parameters with varying operating temperatures

Temperature (K)	J_{sc} (mA cm^{-2})	V_{oc} (V)	P_{max} (W)	FF (%)	Efficiency (%)
290	8.1687	1.5709	49.674	38.711	4.967
300	8.1695	1.7772	46.644	32.126	4.664
310	8.1699	1.5709	45.221	35.235	4.522
320	8.1690	1.4849	43.690	36.017	4.369

Fig. 12(d) illustrates the variation of FF and η with the SnS absorber thickness. Both parameters show a gradual improvement as the thickness increases from 100 nm to 700 nm, where the FF rises from 77.41% to 81.06% and the efficiency reaches its peak value of 20.99%. This enhancement is attributed to improved light absorption, efficient charge separation, and reduced recombination within the optimal thickness range. However, at 1000 nm, the FF drops sharply to 61.56%, and the efficiency decreases to 15.56%, mainly due to the increased series resistance, enhanced recombination losses, and limited carrier diffusion in the overly thick absorber layer. These results confirm that 700 nm is the optimum SnS thickness for achieving maximum device performance.

5. Conclusion

Global warming and our reliance on hazardous energy sources have intensified the search for environmentally friendly energy

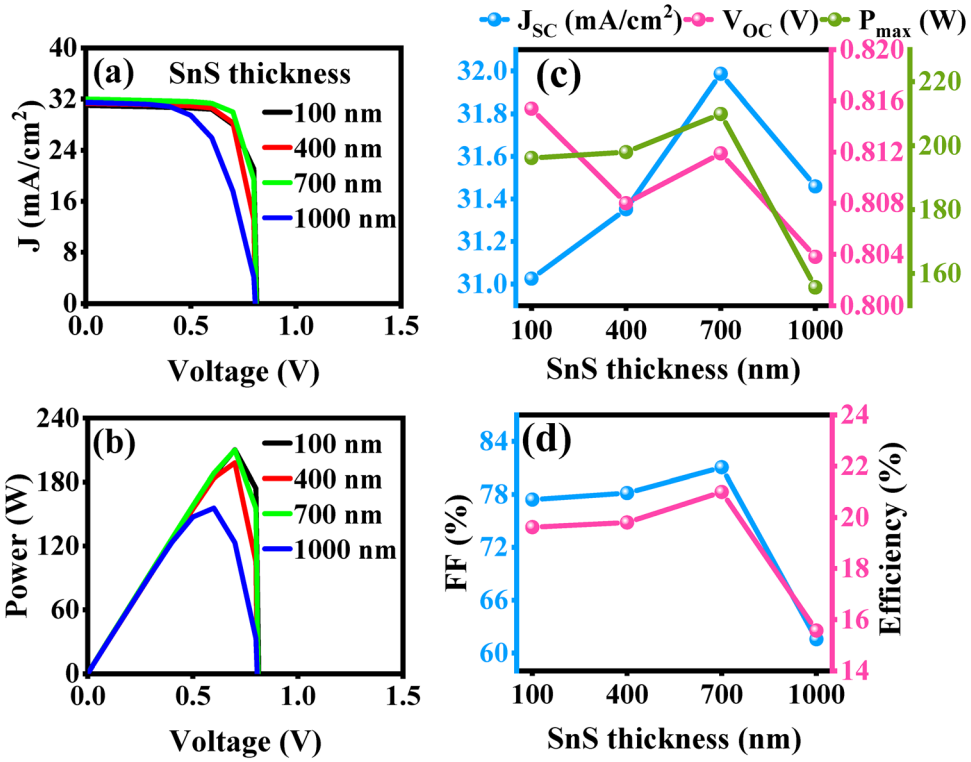

Fig. 12 (a) *J–V* curve and (b) *P–V* curve of the TiO_2/SnS/BFO/Spiro-OMeTAD solar cell. Effect of SnS's thickness on (c) J_{sc}, V_{oc}, P_{max}, and (d) %FF and %efficiency.

alternatives. Among these, solar energy has emerged as a cost-effective, sustainable, and clean solution to meet the rising energy demands of the world's growing population. For decades, researchers have been exploring suitable materials to enhance the stability, cost-efficiency, and performance of solar cells. In this context, perovskite materials, particularly $BiFeO_3$, have gained significant attention as absorber layers due to their multifunctional properties, including room-temperature ferroelectricity and strong permanent polarization, which eliminate the need for conventional p–n junctions. This study employs COMSOL simulation software to model 1D TiO_2/$BiFeO_3$/Spiro-OMeTAD and 1D TiO_2/SnS/$BiFeO_3$/Spiro-OMeTAD solar cell configurations, assuming ideal ohmic front and back metal contacts. Key parameters, such as the thickness and electron affinities of $BiFeO_3$, TiO_2, and Spiro-OMeTAD layers; the density of states in the valence and conduction bands of $BiFeO_3$ and TiO_2; and the operating temperature, were systematically varied to evaluate their impact on the cell's photovoltaic performance. The results demonstrate that the short-circuit current density increases linearly (from 3.697 to 9.004 mA cm^{-2}) with the $BiFeO_3$ thickness (from 50 to 1850 nm), and efficiency reaches a maximum (10.101%) at an optimal thickness of nearly 600 nm. However, efficiency decreases (from 4.881% to 4.876%) with increased TiO_2 thickness (from 10 to 150 nm), while power output and efficiency steadily rise (ranging from 101 to 103.45 W and 10.15% to 10.35%) with the thickness of the hole-transport layer (ranging from 10 to 150 nm). For the SnS layer's thickness, at 700 nm, the device showed a maximum efficiency of 20.99% in the TiO_2/SnS/$BiFeO_3$/Spiro-OMeTAD configuration. The density of states in BFO has a decreasing impact on efficiency and reduces the open-circuit voltage (from 1.99 to 1.235 V), confirming the inverse relation between them, while an increase in the density of states in the ETL leads to an increase in efficiency (from 6.08% to 10.88%). Additionally, increasing the electron affinity of $BiFeO_3$ (from 3.3 to 3.5 eV) decreases the fill factor (from 52.987% to 35.411%), while increasing the electron affinity of TiO_2 (3.5 to 3.7 eV) enhances the open-circuit voltage (1.49 to 1.63 V), and increasing that of Spiro improves the power output (48.78 to 78.32 W). However, a rise in the device's operating temperature (from 290 to 310 K) reduces the overall efficiency (from 4.96% to 4.36%) of the solar cell. This study aids the optimization of material properties and device parameters for experimental purposes and highlights the potential of $BiFeO_3$-based perovskite materials as potential candidates for next-generation photovoltaic applications.

Conflicts of interest

The authors declare that there are no financial or any other types of conflicts of interest to be declared for this submission.

Data availability

Data will be made available on request.

Acknowledgements

The authors acknowledge partial support from University of the Punjab, Lahore, Research Grant for the year 2024–25.

References

1 J. Ajayan, D. Nirmal, P. Mohankumar, M. Saravanan, M. Jagadesh and L. Arivazhagan, A review of photovoltaic performance of organic/inorganic solar cells for future renewable and sustainable energy technologies, *Superlattices Microstruct.*, 2020, **143**, 106549.

2 O. A. Al-Shahri, F. B. Ismail, M. A. Hannan, M. H. Lipu, A. Q. Al-Shetwi, R. A. Begum, N. F. Al-Muhsen and E. Soujeri, Solar photovoltaic energy optimization methods, challenges and issues: A comprehensive review, *J. Cleaner Prod.*, 2021, **284**, 125465.

3 B. P. Singh, S. K. Goyal and P. Kumar, Solar PV cell materials and technologies: Analyzing the recent developments, *Mater. Today: Proc.*, 2021, **43**, 2843–2849.

4 P. Sahoo, C. Tiwari, S. Kukreti and A. Dixit, All oxide lead-free bismuth ferrite perovskite absorber based FTO/ZnO/$BiFeO_3$/Au solar cell with efficiency $\sim$ 12%: First principle material and macroscopic device simulation studies, *J. Alloys Compd.*, 2024, **981**, 173599.

5 J. Chen, H. Dong, J. Li, X. Zhu, J. Xu, F. Pan, R. Xu, J. Xi, B. Jiao, X. Hou and Z. Wu, Solar cell efficiency exceeding 25% through Rb-based perovskitoid scaffold stabilizing the buried perovskite surface, *ACS Energy Lett.*, 2022, **7**(10), 3685–3694.

6 J. Zhang, X. Li, L. Wang, J. Yu, S. Wageh and A. A. Al-Ghamdi, Enhanced performance of $CH_3NH_3PbI_3$ perovskite solar cells by excess halide modification, *Appl. Surf. Sci.*, 2021, **564**, 150464.

7 R. Wang, M. Mujahid, Y. Duan, Z. K. Wang, J. Xue and Y. Yang, A review of perovskites solar cell stability, *Adv. Funct. Mater.*, 2019, **29**(47), 1808843.

8 M. M. Seyfouri and D. Wang, Recent progress in bismuth ferrite-based thin films as a promising photovoltaic material, *Crit. Rev. Solid State Mater. Sci.*, 2021, **46**(2), 83–108.

9 X. Han, Y. Ji and Y. Yang, Ferroelectric photovoltaic materials and devices, *Adv. Funct. Mater.*, 2022, **32**(14), 2109625.

10 R. Taheri-Ledari, F. Ganjali, S. Zarei-Shokat, M. Saeidirad, F. Ansari, M. Forouzandeh-Malati, F. Hassanzadeh-Afruzi, S. M. Hashemi and A. Maleki, A review of metal-free organic halide perovskite: future directions for the next generation of solar cells, *Energy Fuels*, 2022, **36**(18), 10702–10720.

11 H. Li, F. Li, Z. Shen, S. T. Han, J. Chen, C. Dong and M. Wang, Photoferroelectric perovskite solar cells: Principles, advances and insights, *Nano Today*, 2021, **37**, 101062.

12 D. F. Li, X. H. Deng, Y. X. Ma, D. S. Liu, X. F. Huang, X. F. Zhao, W. T. Chen and Y. Sui, A near-room-temperature hybrid organic–inorganic lead halide perovskite ferroelectric $[BrCH_2CH_2N(CH_3)_3][PbBr_3]$ and its flexible composite film, *J. Phys. Chem. C*, 2021, **126**(1), 728–736.

13 Z. Sun, J. Wei, S. Song, M. Xiahou, A. Cao, J. Zhang, Y. Yuanfeng, G. Chen and Y. Chen, Multiple strategies to greatly enhance the photovoltaic characteristics of $BiFeO_3$-based films, *Inorg. Chem. Front.*, 2024, **11**(15), 4780–4793.

14 G. Chen, J. Chen, W. Pei, Y. Lu, Q. Zhang, Q. Zhang and Y. He, Bismuth ferrite materials for solar cells: current status and prospects, *Mater. Res. Bull.*, 2019, **110**, 39–49.

15 A. Abdelsamie, L. You, L. Wang, S. Li, M. Gu and J. Wang, Crossover between bulk and interface photovoltaic mechanisms in a ferroelectric vertical heterostructure, *Phys. Rev. Appl.*, 2022, **17**(2), 024047.

16 Y. P. Jiang, H. C. Zhou, X. G. Tang, W. H. Li, X. B. Guo, Z. H. Tang and Q. X. Liu, Enhanced and controllable ferroelectric photovoltaic effects in $Bi_4Ti_3O_{12}/TiO_2$ composite films, *J. Electron. Mater.*, 2023, **52**(1), 188–195.

17 S. Das, S. Ghara, P. Mahadevan, A. Sundaresan, J. Gopalakrishnan and D. D. Sarma, Designing a lower band gap bulk ferroelectric material with a sizable polarization at room temperature, *ACS Energy Lett.*, 2018, **3**(5), 1176–1182.

18 M. U. Salman, U. Waqas, A. Quader, S. M. Ramay, M. O. U. Rehman and S. Atiq, Concurrent existence of magnetoelectric coupling and electro-optic Kerr effect in perovskite-based ternary composites for energy reservoirs, *J. Alloys Compd.*, 2024, **976**, 173217.

19 E. Gradauskaite, P. Meisenheimer, M. Müller, J. Heron and M. Trassin, Multiferroic heterostructures for spintronics, *Phys. Sci. Rev.*, 2021, **6**(2), 20190072.

20 T. Taniyama, Y. Gohda, K. Hamaya and T. Kimura, Artificial multiferroic heterostructures—electric field effects and their perspectives, *Sci. Technol. Adv. Mater.*, 2024, **25**(1), 2412970.

21 J. W. Zhang, W. Deng, Z. Ye, S. Diaham, C. Putson, X. Zhou, J. Hu, Z. Yin and R. Jia, Aging phenomena of backsheet materials of photovoltaic systems for future zero-carbon energy and the improvement pathway, *J. Mater. Sci. Technol.*, 2023, **153**, 106–119.

22 Y. Liu, Y. Wang, J. Ma, S. Li, H. Pan, C. W. Nan and Y. H. Lin, Controllable electrical, magnetoelectric and optical properties of $BiFeO_3$ via domain engineering, *Prog. Mater. Sci.*, 2022, **127**, 100943.

23 Z. Li, Y. Zhao, W. L. Li, R. Song, W. Zhao, Z. Wang, Y. Peng and W. D. Fei, Photovoltaic effect induced by self-polarization in $BiFeO_3$ films, *J. Phys. Chem. C*, 2021, **125**(17), 9411–9418.

24 S. Valsalakumar, A. Roy, T. K. Mallick, J. Hinshelwood and S. Sundaram, An Overview of Current Printing Technologies for Large-Scale Perovskite Solar Cell Development, *Energies*, 2022, **16**(1), 190.

25 S. Akel, A. Kulkarni, U. Rau and T. Kirchartz, Relevance of long diffusion lengths for efficient halide perovskite solar cells, *PRX Energy*, 2023, **2**(1), 013004.

26 A. Raj, M. Kumar, A. Kumar, K. Singh, S. Sharma, R. C. Singh, M. S. Pawar, M. Z. A. Yahya and A. Anshul, Comparative analysis of 'La'modified $BiFeO_3$-based perovskite solar cell devices for high conversion efficiency, *Ceram. Int.*, 2023, **49**(1), 1317–1327.

27 D. Misiurev, P. Kaspar and V. Holcman, Brief theoretical overview of Bi-Fe-O based thin films, *Materials*, 2022, **15**(24), 8719.

28 A. B. Martínez, P. Grysan, S. Girod, S. Glinsek and T. Granzow, Direct evidence for bulk photovoltaic charge transport in a ferroelectric polycrystalline film, *Sci. Mater.*, 2022, **211**, 114498.
29 M. Teuschel, P. Heyes, S. Horvath, C. Novotny and A. Rusconi Clerici, Temperature stable piezoelectric imprint of epitaxial grown PZT for zero-bias driving MEMS actuator operation, *Micromachines*, 2022, **13**(10), 1705.
30 K. Y. Liang, Y. F. Wang, Z. Yang, S. P. Zhang, S. Y. Jia and J. H. Zeng, Above-band-gap voltage from oriented bismuth ferrite ceramic photovoltaic cells, *ACS Appl. Energy Mater.*, 2021, **4**(11), 12703–12708.
31 A. Gholizadeh and S. Hosseini, Effect of heavy rare-earth substitution on physical properties of $BiFeO_3$ thin films and their photocatalytic application, *J. Am. Ceram. Soc.*, 2024, **107**(6), 4209–4222.
32 H. Mana-ay, C. S. Chen, R. R. Chien, C. S. Tu and P. Y. Chen, Achieving high microscale photoconductivity in Gd-modified bismuth ferrite via modulating ferroelectric polarization, *J. Mater. Chem. C*, 2024, **12**(30), 11529–11539.
33 J. Lin, Y. Chen, H. Wang, B. Tian, Y. Chen, Z. Zhou, F. Yue, R. Huang, C. G. Duan, J. Chu and L. Sun, Unveiling the Anomalous Photovoltaic Effect of Ferroelectric Domain Walls in $BiFeO_3$ Thin Films, *Phys. Rev. Appl.*, 2023, **19**(2), 024050.
34 J. Deng, B. Huang, W. Li, L. Zhang, S. Y. Jeong, S. Huang, S. Zhang, F. Wu, X. Xu, G. Zou and L. Chen, Ferroelectric polymer drives performance enhancement of non-fullerene organic solar cells, *Angew. Chem., Int. Ed.*, 2022, **61**(25), e202202177.
35 A. Singh, C. Prakash, P. Sahoo and A. Dixit, $BiFeO_3$ perovskite-based all oxide ambient stable spectrally selective absorber coatings for solar thermal application, *Sustainable Energy Fuels*, 2024, **8**(12), 2762–2776.
36 A. M. Afzal, Y. Javed, S. Hussain, A. Ali, M. Z. Yaqoob and S. Mumtaz, Enhancement in photovoltaic properties of bismuth ferrite/zinc oxide heterostructure solar cell device with graphene/indium tin oxide hybrid electrodes, *Ceram. Int.*, 2020, **46**(7), 9161–9169.
37 A. Tuluk, H. Brouwer and S. van der Zwaag, Controlling the Oxygen Defects Concentration in a Pure $BiFeO_3$ Bulk Ceramic, *Materials*, 2022, **15**(19), 6509.
38 C. Gumiel and D. G. Calatayud, Thin film processing of multiferroic $BiFeO_3$: From sophistication to simplicity. A review, *Bol. Soc. Esp. Ceram. Vidrio*, 2022, **61**(6), 708–732.
39 N. A. Spaldin, I. Efe, M. D. Rossell and C. Gattinoni, Layer and spontaneous polarizations in perovskite oxides and their interplay in multiferroic bismuth ferrite, *J. Chem. Phys.*, 2021, **154**, 15.
40 C. Wang, Y. Song, L. Wu, C. Xue, H. Feng, H. Li, J. Song, X. Zhang, B. Zou and K. Zhu, Structure and ferroelectric photovoltaic effect modulation in the epitaxial $BiFeO_3$/$La_{0.5}Sr_{0.5}CO_3$ heterostructures, *Micro Nanostruct.*, 2024, **195**, 207956.
41 N. Chelil, M. Sahnoun, Z. Benhalima, R. Larbi and S. M. Eldin, Insights into the relationship between ferroelectric and photovoltaic properties in $CsGeI_3$ for solar energy conversion, *RSC Adv.*, 2023, **13**(3), 1955–1963.
42 W. Pei, J. Chen, D. You, Q. Zhang, M. Li, Y. Lu, Z. Fu and Y. He, Enhanced photovoltaic effect in Ca and Mn co-doped $BiFeO_3$ epitaxial thin films, *Appl. Surf. Sci.*, 2020, **530**, 147194.
43 A. Ray, T. Basu, B. Behera, M. Kumar, R. Thapa and P. Nayak, Role of Gd-doping in conduction mechanism of BFO-PZO nanocrystalline composites: experimental and first-principles studies, *J. Alloys Compd.*, 2018, **768**, 198–213.
44 R. Gupta, S. P. Singh, R. Walia, V. Kumar and V. Verma, Modification in photovoltaic and photocatalytic properties of bismuth ferrites by tailoring band-gap and ferroelectric properties, *J. Alloys Compd.*, 2022, **908**, 164602.
45 X. Yin, C. Chen, Z. Fan, M. Qin, M. Zeng, X. Lu, G. Zhou, X. Gao, D. Chen and J. M. Liu, Coexistence of multiple morphotropic phase boundaries in strained La-doped $BiFeO_3$ thin films, *Mater. Today Phys.*, 2021, **17**, 100345.
46 R. Dhanalakshmi, N. V. Giridharan and J. C. Denardin, Magnetic Field-Assisted Photocatalytic Degradation of Organic Pollutants over $Bi_{1-x}R_xFeO_3$ (R= Ce, Tb; x= 0.00, 0.05, 0.10 and 0.15) Nanostructures, *Materials*, 2021, **14**(15), 4079.
47 M. Čebela, D. Zagorac, I. Popov, F. Torić, T. Klaser, Ž. Skoko and D. Pajić, Enhancement of weak ferromagnetism, exotic structure prediction and diverse electronic properties in holmium substituted multiferroic bismuth ferrite, *Phys. Chem. Chem. Phys.*, 2023, **25**(33), 22345–22358.
48 C. Tian, Q. Yao, Z. Tong, G. Rao, J. Deng, Z. Wang, J. Wang, H. Zhou and J. Zhao, The influence of Nd substitution on microstructural, magnetic, and microwave absorption properties of $BiFeO_3$ nanopowders, *J. Alloys Compd.*, 2021, **859**, 157757.
49 M. Khan, M. A. Iqbal, M. Malik, S. U. M. Hashmi, S. Bakhsh, M. Sohail, M. T. Qamar, M. Al-Bahrani, R. Y. Capangpangan, A. C. Alguno and J. R. Choi, Improving the efficiency of dye-sensitized solar cells based on rare-earth metal modified bismuth ferrites, *Sci. Rep.*, 2023, **13**(1), 3123.
50 A. Sunny, S. Rahman, M. Khatun and S. R. A. Ahmed, Numerical study of high performance HTL-free $CH_3NH_3SnI_3$-based perovskite solar cell by SCAPS-1D, *AIP Adv.*, 2021, **11**(6), 065102.
51 G. T. Tractz, S. R. M. Antunes and P. R. P. Rodrigues, Nb/TiO_2 oxides: A study of synthesis and electron transport mechanism as an ETL in a solar device, *J. Photochem. Photobiol., A*, 2023, **444**, 114899.
52 J. Y. Kim, J. W. Lee, H. S. Jung, H. Shin and N. G. Park, High-efficiency perovskite solar cells, *Chem. Rev.*, 2020, **120**(15), 7867–7918.
53 N. S. Kumar and K. C. B. Naidu, A review on perovskite solar cells (PSCs), materials and applications, *J. Materiomics*, 2021, **7**(5), 940–956.
54 M. K. Hossain, D. P. Samajdar, R. C. Das, A. A. Arnab, M. F. Rahman, M. H. K. Rubel and M. K. Mohammed, Design and simulation of Cs_2BiAgI_6 double perovskite solar cells with different electron transport layers for efficiency enhancement, *Energy Fuels*, 2023, **37**(5), 3957–3979.

55 V. Sebastian and J. Kurian, Simulation and optimization studies on $CsPbI_3$ based inorganic perovskite solar cells, *Sol. Energy*, 2021, **221**, 99–108.
56 A. K. Singh, S. Srivastava, A. Mahapatra, J. K. Baral and B. Pradhan, Performance optimization of lead free-$MASnI_3$ based solar cell with 27% efficiency by numerical simulation, *Opt. Mater.*, 2021, **117**, 111193.
57 I. M. De Los Santos, H. J. Cortina-Marrero, M. A. Ruíz-Sánchez, L. Hechavarría-Difur, F. J. Sánchez-Rodríguez, M. Courel and H. Hu, Optimization of $CH_3NH_3PbI_3$ perovskite solar cells: A theoretical and experimental study, *Sol. Energy*, 2020, **199**, 198–205.
58 S. Karthick, S. Velumani and J. Bouclé, Experimental and SCAPS simulated formamidinium perovskite solar cells: A comparison of device performance, *Sol. Energy*, 2020, **205**, 349–357.
59 M. Carlini, S. J. McCormack, S. Castellucci, A. Ortega, M. Rotondo and A. Mennuni, Modelling and numerical simulation for an innovative compound solar concentrator: Thermal analysis by FEM approach, *Energies*, 2020, **13**(3), 548.
60 S. Zandi, P. Saxena, M. Razaghi and N. E. Gorji, Simulation of CZTSSe thin-film solar cells in COMSOL: Three-dimensional optical, electrical, and thermal models, *IEEE J. Photovolt.*, 2020, **10**(5), 1503–1507.
61 N. Dehghani, A. Jamekhorshid, T. Jalali and S. Osfouri, Numerical modeling of charge transfer and recombination kinetics in the dye-sensitized solar cell: Conceptual integration of optics, electricity, and electrochemistry, *Renewable Energy*, 2024, **239**, 122150.
62 D. Abdel, A. Glitzky and M. Liero, Analysis of a drift-diffusion model for perovskite solar cells, *Discrete Contin. Dyn. Syst. B*, 2025, **30**(1), 99–131.
63 W. Clarke, M. J. Wolf, A. Walker and G. Richardson, Charge transport modelling of perovskite solar cells accounting for non-Boltzmann statistics in organic and highly-doped transport layers, *J. Phys. Energy*, 2023, **5**(2), 025007.
64 D. K. Shah, K. C. Devendra, M. Muddassir, M. S. Akhtar, C. Y. Kim and O. B. Yang, A simulation approach for investigating the performances of cadmium telluride solar cells using doping concentrations, carrier lifetimes, thickness of layers, and band gaps, *Sol. Energy*, 2021, **216**, 259–265.
65 T. Song, D. J. Friedman and N. Kopidakis, Comprehensive performance calibration guidance for perovskites and other emerging solar cells, *Adv. Energy Mater.*, 2021, **11**(23), 2100728.
66 Y. K. Karmani, M. Bilal, M. U. Salman, M. Ameen, M. Luqman, S. M. Ramay, M. Younis and S. Atiq, Correlation between trap-assisted non-radiative recombination losses and thermal agitation in SnS-based solar cell: A state-of-the-art computational analysis, *Mater. Sci. Eng. B*, 2025, **321**, 118484.
67 M. Kumar, S. K. Pundir and D. V. Singh, Effect on green energy conversion and stability with 'Er'modification in multiferroic based perovskite solar cell devices, *Mater. Today Commun.*, 2024, **38**, 107841.
68 Y. Li, J. Wei, Z. Sun, T. Yang, Z. Liu, G. Chen, L. Zhao and Z. Cheng, Greatly enhanced photocurrent density in bismuth ferrite films by Localized Surface Plasmon Resonance effect, *Appl. Surf. Sci.*, 2022, **583**, 152571.
69 T. Nakamura, W. Yanwachirakul, M. Imaizumi, M. Sugiyama, H. Akiyama and Y. Okada, Reducing Shockley–Read–Hall recombination losses in the depletion region of a solar cell by using a wide-gap emitter layer, *J. Appl. Phys.*, 2021, **130**(15), 153102.
70 Q. Fatima, A. A. Haidry, H. Zhang, A. El Jery and M. Aldrdery, A critical review on advancement and challenges in using TiO_2 as electron transport layer for perovskite solar cell, *Mater. Today Sustainability*, 2024, **27**, 100857.
71 S. Dabas, M. Kumar, D. V. Singh and P. Kumar, Cutting-edge technologies and recent modernization on multifunctional perovskite materials for green energy conversion and spintronic applications, *Mater. Lett.*, 2024, **377**, 137389.
72 G. Tumen-Ulzii, T. Matsushima and C. Adachi, Mini-review on efficiency and stability of perovskite solar cells with Spiro-OMeTAD hole transport layer: Recent progress and perspectives, *Energy Fuels*, 2021, **35**(23), 18915–18927.
73 Y. Ait-Wahmane, H. Mouhib, B. Ydir, A. Ait Hssi, L. Atourki, A. Ihlal and K. Bouabid, Comparison study between ZnO and TiO_2 in CuO based solar cell using SCAPS-1D, *Mater. Today: Proc.*, 2022, **52**, 166–171.
74 M. U. Salman, M. Bilal, Y. K. Karmani, U. Ali, S. M. Ramay, M. Younis and S. Atiq, Influence of acceptor/donor densities and layer thicknesses on the efficiency of 2D ZnO/BFO/spiro-OMeTAD perovskite solar cells: a COMSOL simulation-based optimization, *J. Mater. Chem. A*, 2025, **13**(20), 15057–15066.
75 M. M. Mudassar, M. Arshad, M. U. Salman, A. Mahmood, W. Al-Masry, M. Asim and S. Atiq, Significance of the direct relation between the fill factor and hole transport layer thickness in perovskite-based solar cells for green energies, *RSC Adv.*, 2025, **15**(40), 33830–33843.
76 M. Kumar, D. V. Singh, S. Sharma, D. K. Dwivedi, A. Anshul, M. K. Hossain and S. K. Pundir, Investigations on interfacial complex dynamic processes of Er-$BiFeO_3$ based perovskite solar cell heterostructures, *Inorg. Chem. Commun.*, 2025, **171**, 113587.
77 T. M. Mukametkali, B. R. Ilyassov, A. K. Aimukhanov, T. M. Serikov, A. S. Baltabekov, L. S. Aldasheva and A. K. Zeinidenov, Effect of the TiO_2 electron transport layer thickness on charge transfer processes in perovskite solar cells, *Phys. B*, 2023, **659**, 414784.
78 I. Alam and M. A. Ashraf, Effect of different device parameters on tin-based perovskite solar cell coupled with In_2S_3 electron transport layer and CuSCN and Spiro-OMeTAD alternative hole transport layers for high-efficiency performance, *Energy Sources, Part A*, 2024, **46**(1), 17080–17096.
79 D. K. Dwivedi, Modeling of CZTSSe solar photovoltaic cell for window layer optimization, *Optik*, 2020, **222**, 165407.
80 R. Jeyakumar, A. Bag, R. Nekovei and R. Radhakrishnan, Influence of electron transport layer (TiO_2) thickness and its

doping density on the performance of $CH_3NH_3PbI_3$-based planar perovskite solar cells, *J. Electron. Mater.*, 2020, **49**(6), 3533–3539.

81 H. Chen, Z. Q. Li, B. Sun and X. D. Feng, Towards high-efficiency planar heterojunction antimony sulfide solar cells, *Opt. Mater.*, 2021, **121**, 111556.

82 F. M. Rombach, S. A. Haque and T. J. Macdonald, Lessons learned from spiro-OMeTAD and PTAA in perovskite solar cells, *Energy Environ. Sci.*, 2021, **14**(10), 5161–5190.

83 R. Garain, A. Basak and U. P. Singh, Study of thickness and temperature dependence on the performance of SnS based solar cell by SCAPS-1D, *Mater. Today: Proc.*, 2021, **39**, 1833–1837.